Applicability Analysis of Potential Landslide Identification by InSAR in Alpine-Canyon Terrain—Case Study on Yalong River

Keren Dai, Ye Feng, Guanchen Zhuo, Yongbo Tie, Jin Deng, Timo Balz, and Zhenhong Li

***Abstract*—Landslides occur frequently in the western mountainous areas of China, causing huge losses every year. InSAR technology can efficiently and accurately identify potential landslides and is a powerful tool for landslide hazards mitigation. However, the successful application of InSAR technology is limited by several factors, such as geometric distortion and dense vegetation, especially in the area with alpine-canyon terrain. This study investigates the applicability of InSAR observations in identifying potential landslides of the middle section of the Yalong River, which is a typical alpine-canyon terrain area. Using time-series InSAR Sentinel-1 datasets, we detect six potential landslides, which are verified and analyzed by using optical remote sensing images. Then, the applicability analysis is performed considering geometric distortion and band suitability. The results reveal that combining ascending and descending data can increase the detectable area (not in the geometric distortion) from 70% to 92.9%. The comparison of the performance of *C*-band and *L*-band data in identifying potential landslides shows that the latter is able to detect potential landslides with high vegetation coverage but it may miss the area with slight displacement. This study demonstrates the use of InSAR for potential landslide identification in alpine-canyon terrain areas and reveals its applicability, which provides a deep understanding of SAR data selection and would play an important role in the InSAR-based landslide geohazard mitigation application.**

***Index Terms*—Applicability analysis, geometric distortion, time-series InSAR, Yalong River.**

Manuscript received 27 July 2022; revised 1 November 2022; accepted 4 December 2022. Date of publication 20 December 2022; date of current version 13 January 2023. This work was supported in part by the fellowship of the China Postdoctoral Science Foundation under Grant 2020M673322, in part by the Public Geological Survey Project of China Geological Survey under Grant DD20190640, in part by the National Natural Science Foundation of China Major Program under Grant 41941019, in part by the National Key R&D Program of China under Grant 2021YFB3901403, in part by the State Key Laboratory of Geohazard Prevention and Geoenvironment Protection Independent Research Project under Grant SKLGP2020Z012, and in part by a project on the identification and monitoring of potential geological hazards with remote sensing in Sichuan Province under Grant 510201202076888. *(Corresponding author: Zhenhong Li.)*

Keren Dai is with the College of Geological Engineering and Geomatics, Chang'an University, Xi'an 710054, China, also with the Key Laboratory of Western China's Mineral Resource and Geological Engineering, Ministry of Education, Xi'an 710054, China, also with the State Key Laboratory of Geohazard Prevention and Geoenvironment Protection, Chengdu University of Technology, Chengdu 610059, China, and also with the College of Earth Science, Chengdu University of Technology, Chengdu 610059, China (e-mail: daikeren17@cdut.edu.cn).

Ye Feng is with the Sichuan Land Consolidation and Rehabilitation, Chengdu 610059, China (e-mail: iloveinsar@foxmail.com).

Guanchen Zhuo and Jin Deng are with the State Key Laboratory of Geohazard Prevention and Geoenvironment Protection, Chengdu University of Technology, Chengdu 610059, China, and also with the College of Earth Science, Chengdu University of Technology, Chengdu 610059, China (e-mail: zhuoguanchen_rs@foxmail.com; dengjin@stu.cdut.edu.cn).

Yongbo Tie is with the China Geological Survey Chengdu Geological Survey Center, Chengdu 610059, China (e-mail: tyb2009@qq.com).

Timo Balz is with the State Key Laboratory of Information Engineering in Surveying, Mapping and Remote Sensing (LIESMARS), Wuhan University, Wuhan 430079, China (e-mail: balz@whu.edu.cn).

Zhenhong Li is with the College of Geological Engineering and Geomatics, Chang'an University, Xi'an 710054, China, and also with the Key Laboratory of Western China's Mineral Resource and Geological Engineering, Ministry of Education, Xi'an 710054, China (e-mail: zhenhong.li@chd.edu.cn).

Digital Object Identifier 10.1109/JSTARS.2022.3228948

I. Introduction

In western Sichuan, China, the uplift of the Tibetan Plateau and the sharp undercutting of river valleys have formed canyon terrains, favoring the occurrence of landslides [1]. The Yalong River is located in the transition zone from the Qinghai–Tibet Plateau (QTP) to the Sichuan Basin, with a relative height difference of 2000–3000 m, where the river valley has a "V" shape and is a typical alpine canyon [2]. At present, strong earthquakes together with densely distributed hydropower stations along the river, contribute to increasing landslides and other geohazards in this basin [2], [3], [4], [5].

The areas with the alpine-canyon terrain are usually inaccessible for people, so traditional landslide detection methods have very low accuracy and feasibility [6], [7], [8], [9], [10], [11]. Interferometry Synthetic Aperture Radar (InSAR) technology is featured by wide spatial coverage, high precision, all-weather independence, so it has been successfully used for identifying geological hazards in alpine-canyon terrain [12], [13], [14], [15]. Zhu et al. [16] detected 10 potential landslides in the Bailong River basin by the small baseline subset InSAR (SBAS-InSAR) technology. Sun et al. [17] combined the InSAR time series to monitor the slowly deforming landslides in Zhouqu, Gansu, China. Dai et al. [18] identified eight potential landslide geohazards along the Yalong River using Sentinel-1 data by the SBAS-InSAR technology. The successful application of potential landslide identification in the complex terrain and vegetation coverage by InSAR technology is influenced and limited by several factors, such as geometric distortion and dense vegetation coverage. For example, Liu et al. [19] found that the SAR images in some areas along the Jinsha River corridor were affected by geometrical distortion due to the steep terrain, meaning that some landslides that occurred in these areas might be omitted. Wang et al. [20] used a priori estimation to conduct postprocessing analyses on the reliabilities

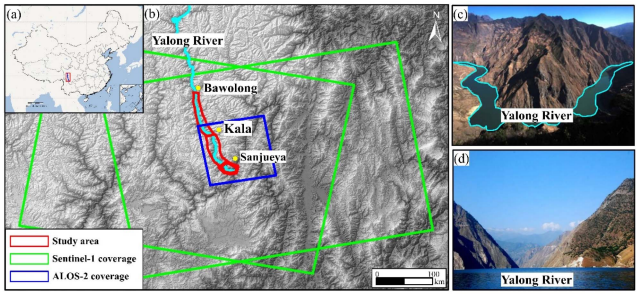

Fig. 1. Study area. (a) Location of the study area. (b) Satellite image coverage. (c) and (d) Topography of a section of the Yalong River.

of the InSAR landslide detection to analyze the InSAR landslide applicability before SAR data processing. Dun et al. [21] investigated the geometric distortion types of the ALOS-1 ascending, Sentinel-1 ascending, and descending data for the Baihetan Reservoir Area and reported that geometric distortions impact the displacement results. Zhu et al. [22] studied the accuracy and reliability of identifying unstable slopes in areas with dense vegetation by Sentinel-1, ALOS-2. Promising application results were acquired in the above study. However, the applicability (e.g., does the monitoring results cover all the slopes? What is the influence from different bands used) is still clear enough. The understanding of InSAR applicability to identify potential landslides in the complex alpine-canyon area is worthy of further studying to meet the requirement of engineering and disaster reduction application.

This study investigates the applicability of InSAR observations in identifying potential landslides in the middle section of the Yalong River, which is a typical alpine canyon. And the applicability analysis is performed considering geometric distortion and wave band suitability by Sentinel-1 and ALOS-2 images. This study demonstrates the use of InSAR for potential landslide identification in alpine-canyon terrain and reveals its applicability in terms of geometric distortion and wave band suitability by Sentinel-1 and ALOS-2 images, providing a deep understanding of SAR data and InSAR performance in alpine-canyon terrain.

II. Study Area and Datasets

The Yalong River is a large tributary of the Jinsha River (one of the major north–south-oriented rivers in the Hengduan Mountains). Most of the Yalong River is in the transition zone from QTP to the Yunnan–Guizhou Plateau and the Sichuan Basin and is also a part of the QTP [2]. The elevation of the entire area decreases from northwest to southeast, and the surface cutting intensifies from north to south. The topography is complex and diverse, including mountains, hills, and river terraces [3] [see Fig. 1(b) and (c)]. The steep slopes and gully beds provide favorable conditions for releasing or converting the potential energy into kinetic energy, thus facilitating the occurrence and acceleration of geological hazards. Therefore, this region is prone to geological hazards, such as landslides, collapses, and mudslides.

TABLE I
Main Parameters of the SAR Data Used in This Study

Parameters	Sentinel-1		ALOS-2
Orbit direction	Ascending	Descending	Ascending
Band	C		L
Wavelength(cm)	5.6		23.6
Azimuth/Range pixel spacing (m)	2.3/13.9		14/2.3
Revisit frequency(d)	12		14
Incidence angle(°)	36.8	39.7	40.54
Azimuth angle (°)	-12.6	-167.4	-16
Acquisition time	2017.09–2019.03	2019.06–2020.12	2018.01–2019.07
Number of data	47	40	10

Two types of spaceborne SAR data are used in this study: *C*-band Sentinel-1 data in the ascending and descending orbits and *L*-band ALOS2-PALSAR2 (referred to as ALOS-2 data hereafter) in the ascending orbit. Table I lists the main parameters of these data.

The temporal baseline and spatial baseline of the interferograms of the ascending Sentinel-1 data are 48 days and 150 m, respectively, and for the Sentinel-1 descending interferograms are 60 days and 160 m, respectively (see Fig. 2). The interferogram of ALOS-2 data has no spatial–temporal baseline threshold, as the images are few and have good coherence. The precise Sentinel-1 orbit data released by European Space Agency was used in the data processing to correct the orbital efforts; ALOS World 3D 30-m Digital Elevation Model (DEM) was used to remove the topography-related phase and assist the geocode processing.

III. Methods

A. SBAS-InSAR Method

The SARscape Modules in ENVI software suite (HARRIS Geospatial Solutions, Broomfield, CO, USA) were used for SBAS-InSAR processing. The SBAS-InSAR technique can effectively reduce the spatiotemporal decoherence by the following process [23].

First, the single look complex (SLC) SAR dataset from the raw data (RAW) and precise orbit determination (POD) were acquired. Connections between the SAR images with good coherence are established to form the interferometric pairs. The interferograms were generated after removing flat and topographic phase components by POD information and external DEM data. The adaptive filter was used to reduce the noise of interferograms. The phase unwrapping was performed on the selected interferograms by the minimum cost flow (MCF) method. Next, to estimate and remove the residual constant phase and the phase ramp in time-series interferometric pairs, the ground control points were selected in the pixel with stable phase (no obvious deformation) and high coherence pixel in the time-series interferometric pairs. Then, the atmospheric phase components

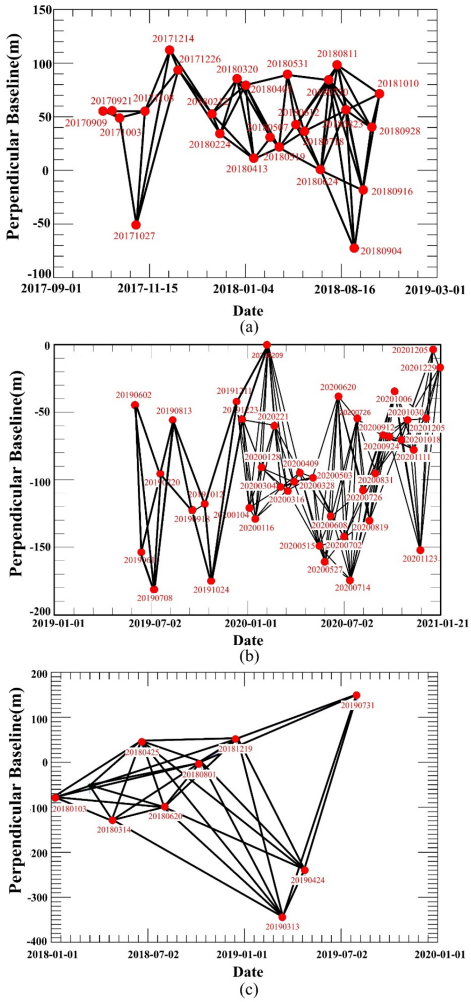

Fig. 2. Spatial and temporal baselines of (a) Sentinel-1 ascending datasets, (b) Sentinel-1 descending datasets, and (c) ALOS-2 ascending datasets.

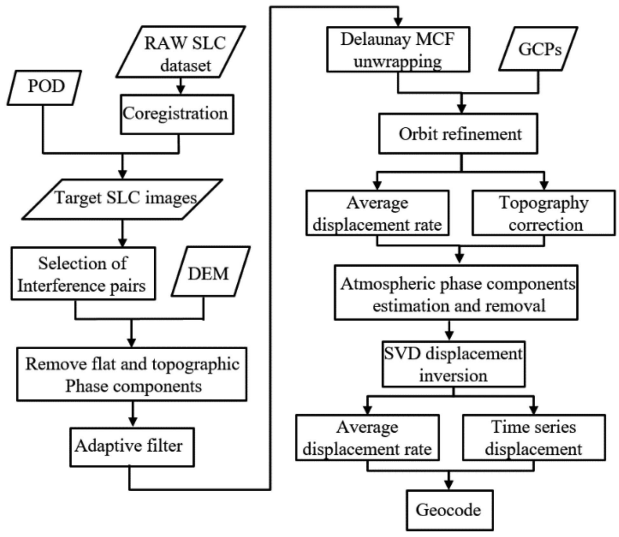

Fig. 3. Flowchart of SBAS-InSAR time-series analysis.

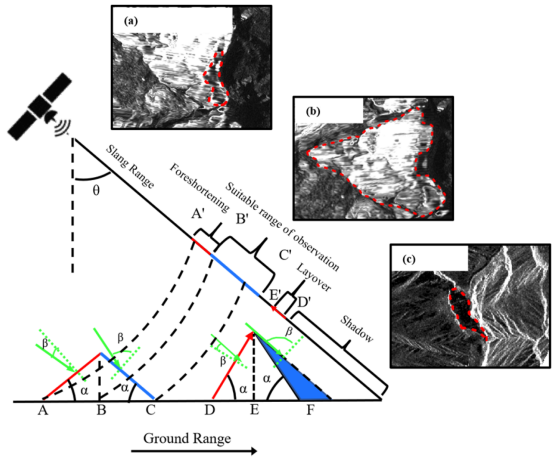

Fig. 4. Geometric distortions on the SAR image. (a) Foreshortening. (b) Layer. (c) Shadow.

were estimated and removed by atmospheric filtering to get the final displacement result in the corrected time series.

Finally, the average displacement rate and the cumulative displacement were estimated by the singular value decomposition method, and these were converted to geographical coordinates for the subsequent analysis. The flowchart is shown in Fig. 3.

B. Geometric Distortion Determination

The SAR images over the alpine-canyon terrain are influenced by geometric distortions due to the side-looking geometries of SAR sensors [17]. Therefore, we use a method based on the local incidence angle to discriminate geometric distortion [24]. The local incidence angle is the angle between the radar incidence direction and the slope normal direction (from the slope normal direction to the radar incidence direction is positive). We establish a relationship between the satellite line-of-sight (LOS) direction and the local incidence angle to classify the SAR observation into four situations: 1) layover, 2) foreshortening, 3) shadow, and 4) suitable for observation [25].

Fig. 4 shows the effects of geometric distortions on the SAR images. For the slope toward the SAR sensor, when the incidence angle θ is larger than the slope angle α, on the image the slope length is shorter than its actual length, resulting in low range resolution. This is the so-called foreshortening effect [i.e., Fig. 4(a)]. The resolution is the lowest when $\theta = \alpha$. In such cases, slope AB is compressed to A′B′ on the SAR image, and the local incidence angle β is smaller than the incidence angle θ. When θ is smaller than α, the slope bottom and top are reversely imaged, known as the layover effect [i.e., Fig. 4(b)]. Generally, the layover slopes are much brighter than other things in the image. In such cases, the local incidence angle β is smaller than 0. For the slopes facing away from the SAR senor, when $90°-\theta$ is larger than α, the range resolution of such slopes is higher than its ground resolution. Obviously, this situation is suitable for SAR observation. At this time, the local incidence angle β is larger than θ and smaller than 90°. However, when α is larger than $90°-\theta$, such steep slopes completely block the SAR signals. This is the shadow effect that shows slopes dark on the SAR image [i.e., Fig. 4(c)]. And the local incidence angle β is larger than 90°.

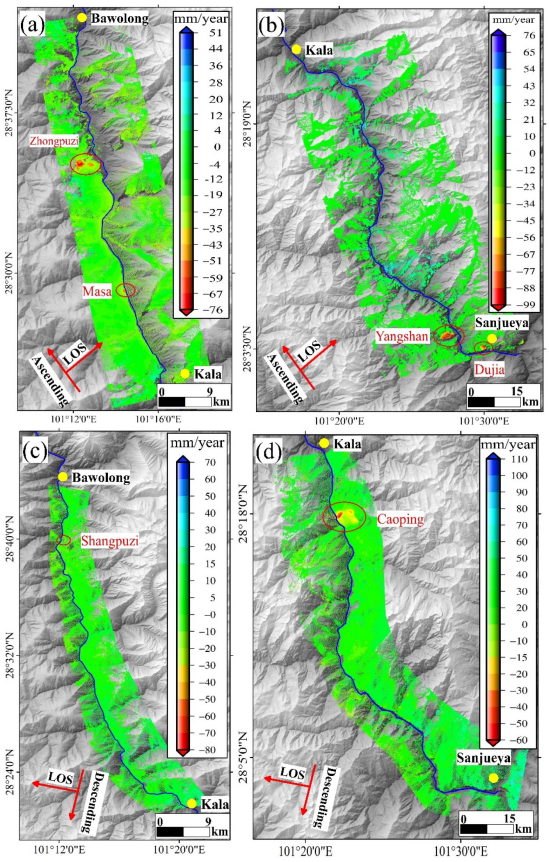

Fig. 5. Displacement velocity map derived from (a) and (b) Sentinel-1 ascending and (c) and (d) descending data. Negative values (red) indicate the motion away from the satellite and positive values (blue) indicate the motions toward the satellite.

C. Coherence Calculation

The coherence coefficient is often used to evaluate the quality of the interferogram pairs [26], [27]. The coherence coefficient ranges between 0 and 1. Zero means no coherence and 1 means the two are identical [28]. The coherence coefficient is calculated by formula

$$\gamma = \frac{\left|\sum s_1(x) \cdot s_2(x)^*\right|}{\sqrt{\sum |s_1(x)|^2 \cdot \sum |s_2(x)|^2}} \tag{1}$$

where $s_1(x)$ is the complex value of the master image and $s_2(x)$ is the complex value of the slave image.

We randomly take one image element as the center to calculate γ according to a set window size. And γ at each point is used for evaluating the quality of the interferometric phase of that image element.

IV. Identification of Potential Landslides by InSAR

A. Overall Identification Results

We monitor the stability of the slopes on both sides of the Yalong River basin using the SBAS-InSAR technology and Sentinel-1 ascending and descending data. The results are shown in Fig. 5.

A total of six slopes undergoing creeping are identified (see Fig. 5), two in section (a) and two in section (b) by ascending data, and one in section (c) and one in section (d) by the descending data. These six slopes have medium–low vegetation coverage, an average elevation greater than 2000 m, and an average slope greater than 55%. During the monitoring period, they all have obvious displacement, with the minimum average displacement rate of 33 mm/y and the maximum average displacement rate of more than 99 mm/y. Influenced by observation geometry and geometric distortion, the identification results of the ascending data are mostly located on the east (right) bank of the Yalong River, and those of the descending data are mainly distributed on the west (left) bank.

B. Analysis and Verification of the Results

We analyze these six slopes in two ways. First, we investigate whether the slopes are located in nongeometric displacement zones by SAR imaging parameters, slope angle, and aspect angle. Second, the InSAR results are compared with the geological data, database of geological hazard sites, literature, and optical image results. The results show that all six slopes are in nongeometric distortion zones, so they can be monitored by InSAR. Some of the slopes are reactivated paleo landslides, and some are caused by human activities. Then, optical remote sensing images of these slopes are used to observe the vegetation coverage, landslide signs, and topographic features. Finally, we confirm that the six slopes have landslide hazard risks.

Fig. 6 shows the spatial distribution of these six slopes in Shangpuzi, Zhongpuzi, Masa, Caoping, Yangshan, and Dujia. The slopes of Shangpuzi, Masa, Yangshan, and Dujia were detected by ascending orbit while Shangpuzi and Caoping were detected by descending orbit (see Table II).

The Shangpuzi slope is located on the east bank of the Yalong River. The elevation of the slope is 1900–2330 m with an average slope gradient of about 60%, and the maximum displacement rate (LOS direction) is 39 mm/y on the upper part of the slope (see Table II). According to optical remote sensing images, significant human engineering activities were observed in the deformation area [see Fig. 6(a-1) and (a-3)]. From the time-series result, the displacement rate of Shangpuzi slope slowed down a little from October 2019 [see Fig. 6(a-4)].

The Zhongpuzi slope is located on the west bank. The elevation of the slope is 1900–3000 m with an average slope gradient of about 60%, and the maximum displacement rate reached up to 73 mm/y (see Table II). An ancient landslide named Baduogou landslide was found by optical remote sensing images [see Fig. 6(b-2)]. The time-series displacement of Zhongpuzi slope is almost linear [see Fig. 6(b-3)].

The Masa slope is located on the west bank. The elevation of the slope is 1900–2500 m with an average slope gradient of about 55%, and the maximum displacement rate is 46 mm/y (see Table II). An ancient landslide named Zhoujia landslide was found by optical remote sensing images [see Fig. 6(c-2)]. The time-series displacement of the Masa slope is near linear [see Fig. 6(c-3)].

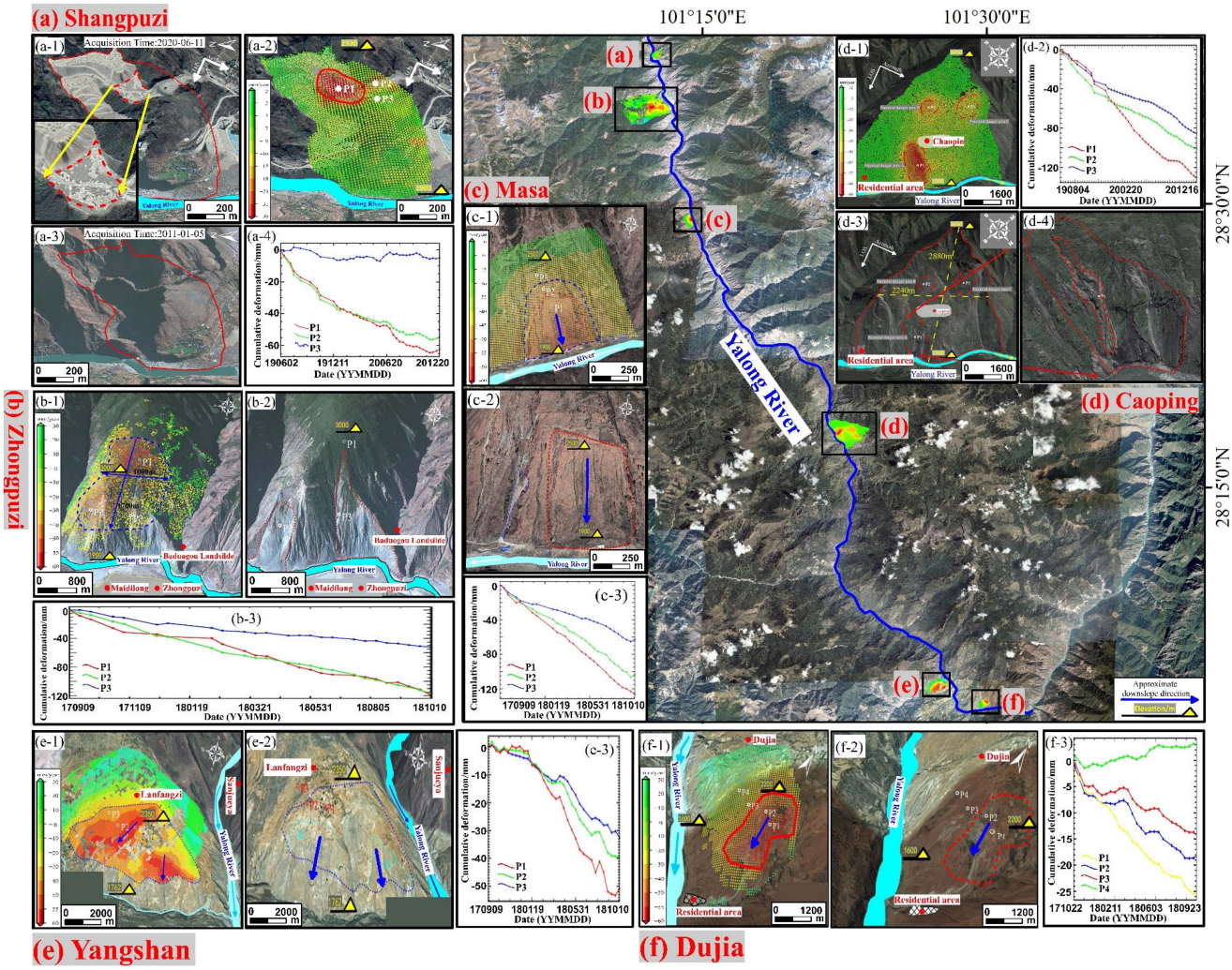

Fig. 6. Spatial distribution of the potential landslides in the study area, and the displacement velocity map and optical remote sensing images in (a-1)–(a-4) Shangpuzi, (b-1)–(b-3) Zhongpuzi, (c-1)–(c-3) Masa, (d-1)–(d-4) Caoping, (e-1)–(e-3) Yangshan (e-1 to e-3), and (f-1)–(f-3) Dujia.

TABLE II
IDENTIFICATION RESULTS OF THE POTENTIAL DISASTER POINTS ALONG THE YALONG RIVER

Orbit	Landslide	Latitude and longitude	Maximum displacement rate (mm/y)	Grades (slope) (%)	Elevation (m)	Topographic features	Space distribution
Ascending	Zhongpuzi	101°12′30″E 28°35′04″N	73	60	1900–3000	Visible ancient landslide	West bank
	Masa	101°14′21″E 28°29′07″N	46	55	1900–2500	Visible ancient landslide	West bank
	Yangshan	101°27′32″E 28°04′18″N	53	62	1762–2350	No obvious features	West bank
	Dujia	101°30′07″E 28°03′31″N	60	55	1600–2200	Visible history collapse	West bank
Descending	Shangpuzi	101°12′30″E 28°35′04″N	39	60	1900–3000	No obvious features	East bank
	Caoping	101°22′38″E 28°17′52″N	99	53	1900–3650	Visible ancient landslide	East bank

The Caoping slope is located on the east bank. The elevation of the slope is 1900–3650 m with an average slope gradient of about 53%. There are three obvious active areas in the slope and the maximum displacement rate reached up to 99 mm/y (see Table II). An ancient landslide named Caoping landslide was found by optical remote sensing images [see Fig. 6(d-3) and (d-4)]. The time-series displacement in the Masa slope is linear [see Fig. 6(d-2)].

The Yangshan slope is located on the west bank. The elevation of the slope is 1726–2350 m with an average slope gradient of about 62%. The maximum displacement rate is 53 mm/y (see Table II). However, there were no obvious displacement signs found by optical remote sensing images [see Fig. 6(e-2)]. The time-series displacement in the slope is accelerating since March 2018 [see Fig. 6(e-3)].

The Dujia slope is located on the west bank. The elevation of the slope is 1600–2200 m with an average slope of about 55%. The maximum displacement rate is 60 mm/y (see Table II). A historic collapse was found by optical remote sensing images [see Fig. 6(f-2)]. The time-series displacement in the slope is accelerating since March 2018 [see Fig. 6(f-3)].

V. Discussion

A. Analysis of the Geometric Distortion Suitability of SAR

Geometric distortion, generated from the SAR side-looking imaging geometry, influences the results. The InSAR measurements acquired from ascending tracks and descending tracks have different geometric distortions in some areas, resulting in inconsistent and even contradictory results. Therefore, when we employ and integrate SAR datasets of different orbits, the effects of geometric distortion of different orbits should be distinguished.

The azimuth and incidence angles of the SAR data covering the study area in this study are shown in Fig. 7. The incidence angles are not constant in the slant range. In this experimental area, the incidence angle of Sentinel-1 ascending data varies between 34.46° and 38.70°, and the azimuth angle varies between 78.23° and 78.31°. If the slope faces the satellite, foreshortening will occur for the slopes between 0° and 38.70°, and layover will occur for the slopes between 38.70° and 90°. If the slope is away from the satellite, the observation is reliable for the slopes with the angles below 51.30°, and shadow will occur if the slope absolute value is greater than 51.30°. The incidence angle of Sentinel-1 descending data varies between 35.96° and 40.01° and the azimuth angle varies between −80.69° and −80.55°. The occurrence of geometric distortion is the same as those of the ascending orbit.

The local incidence angles of the Sentinel-1 ascending and descending orbits are shown in Fig. 8(a) and (b). The local incidence angle for the ascending orbit ranges from −40.14° to 10.78° with a mean value of 36.07°. The descending orbit ranges from −39.45° to 113.75° with a mean value of 38.55°. Using the 30-m resolution DEM from the ALOS satellite, we get the aspect angle and slope angle [see Fig. 8(c) and (d)]. The average slope angle of the study area is 35° and the maximum slope angle is 83°, which is typical for the alpine-canyon terrain.

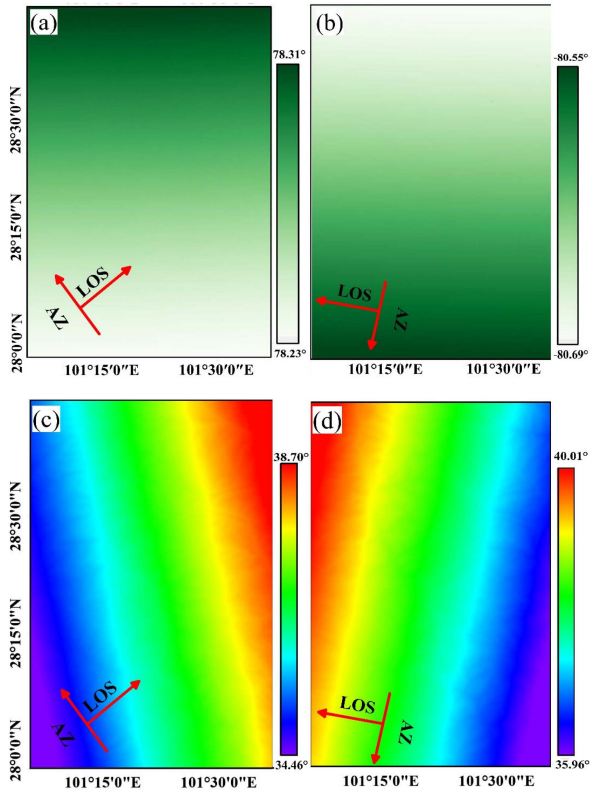

Fig. 7. Azimuth and incidence angles of the SAR data covering the study area. (a) Azimuth angle (Sentinel-1 ascending). (b) Azimuth angle (Sentinel-1 descending). (c) Incidence angle (Sentinel-1 ascending). (d) Incidence angle (Sentinel-1 descending).

In this study, the regions with foreshortening effects and suitable observation are defined as detectable regions, and the regions with layover and shadow are defined as undetectable regions. As Fig. 9(a) shows, in the ascending data results, the detectable area accounts for 71.5% and the nondetectable area accounts for 28.5%. The detectable area on the west bank is larger than that on the east bank because most of the slopes on the west bank face east and the slope is less than 53.2°, which are more suitable for the ascending data detection. As Fig. 9(b) shows, in the descending data results, the detectable area accounts for 74.8%, and the nondetectable area accounts for 25.2%. The detectable area on the east bank is larger than that on the west bank because most of the slopes on the east bank face west and the slopes are less than 50.3°, which are suitable for descending data detection. Generally, using either the ascending or the descending data alone can monitor more than 70% of the study area, and the monitoring areas are complementary.

To achieve a wider detectable range, we can combine the ascending and descending data. As shown in Fig. 10, the area can be observed by both ascending and descending data accounts for 53.4%, which can be used for joint analysis to extract multidimensional displacement. The area that can only be observed by ascending data accounts for 18.1%, mainly distributed on the west bank of the Yalong River. The area that can only be observed by descending data accounts for 21.3%, mainly distributed on

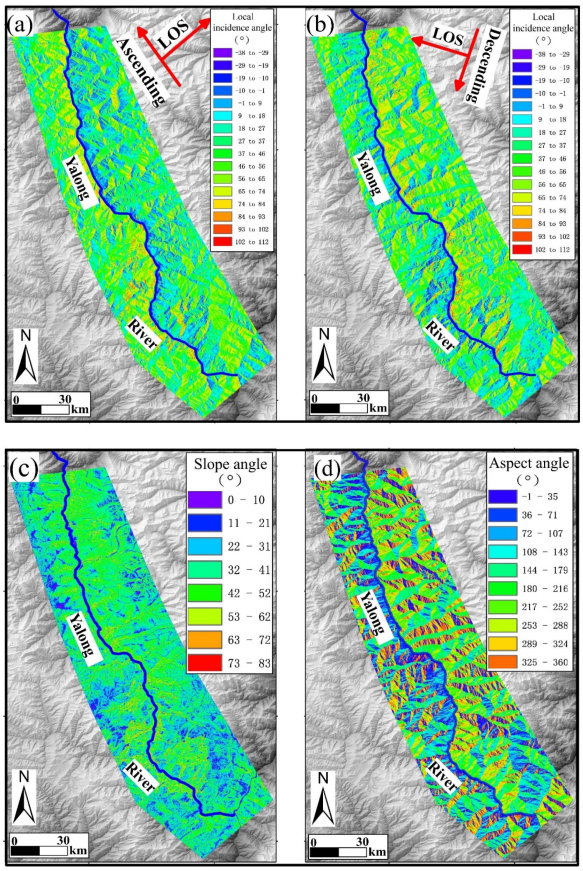

Fig. 8. (a) and (b) Local incidence angle for the Sentinel-1 ascending orbit and descending orbit. (c) and (d) Local terrain slope and aspect angle.

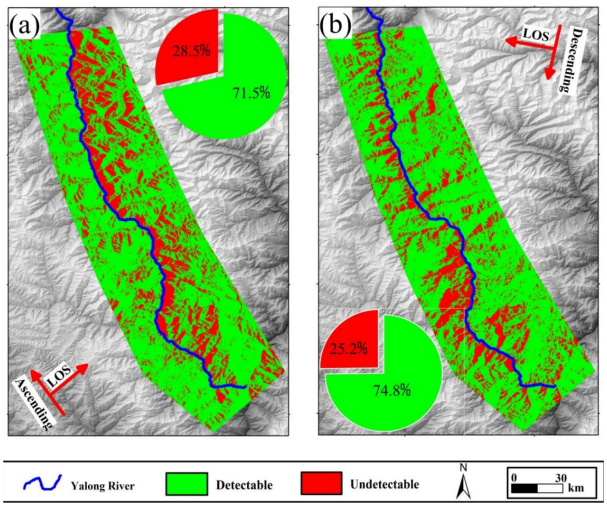

Fig. 9. Areas detected by Sentinel-1 in different tracks. (a) Ascending track. (b) Descending track.

the east bank of the Yalong River. Combining these two data, the detectable area is increased to 92.9%. In the geological hazard identification, for large-scale regions, using a combination of ascending and descending data can reduce the nondetectable area, and for small-scale regions, using the right single-track data is of great importance.

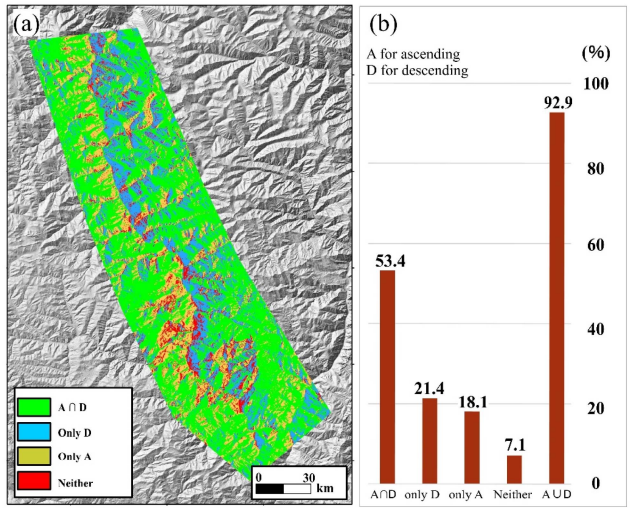

Fig. 10. Regions detected by Sentinel-1 ascending and descending orbits and their proportions. (a) Regional detected results. (b) Proportions of the area under observation. A∪D and A∩D means areas observed by both ascending and descending data, either ascending or descending data, respectively.

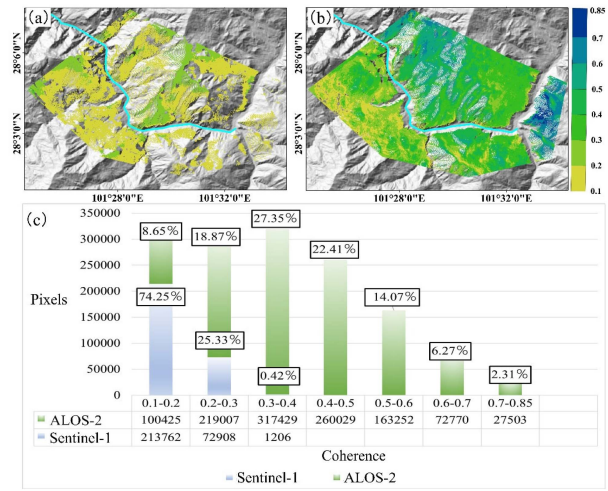

Fig. 11. Coherence distribution of (a) Sentinel-1 data and (b) ALOS-2 data. (c) Coherence statistics.

B. Analysis of the Wave Band Suitability of SAR

1) Overall Comparative Analysis of Coherence: We compare the performance of *C*-band Sentinel-1 data and the *L*-band ALOS-2 data in identifying potential landslides in alpine-canyon terrain. The coherence distribution of the interferogram pairs of these two data is shown in Fig. 11. The same parameters are used in processing. For Sentinel-1 data, the coherence of 74.25% pixels is between 0.1 and 0.2 while for ALOS-2 data, only 8.65% of pixels have the coherence between 0.1 and 0.2 [see Fig. 11(c)]. This result suggests that the coherence of Sentinel-1 data is significantly lower than ALOS-2.

To further analyze the coherence differences of Sentinel-1 and ALOS-2, three regions with different surface vegetation cover were selected. Table III lists the parameters of the interferometric pairs selected for comparison. Because the spatial baseline has a great influence on the coherence, we select the interferometric

TABLE III
COMPARISON OF TYPICAL INTERFERENCE PAIR PARAMETERS

Data source	Sentinel-1	ALOS-2
Acquisition time	2017.09.21–2017.10.15	2018.10.10–2018.12.19
Temporal baseline (d)	24	70
Spatial baseline (m)	-53	52

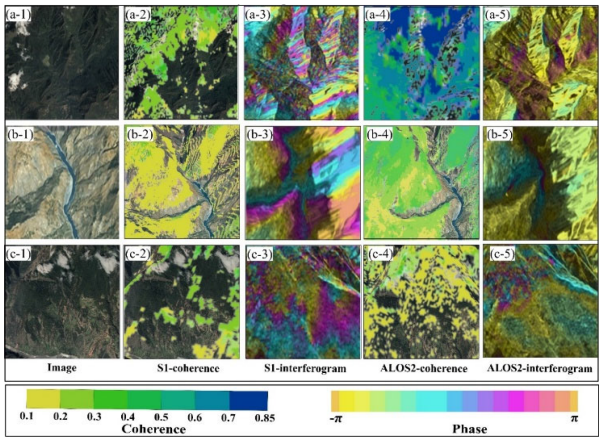

Fig. 12. Comparison of the signal coherence and interferograms of Sentinel-1 data and ALOS-2 data in three regions with different vegetarian cover. (a) Region 1. (b) Region 2. (c) Region 3.

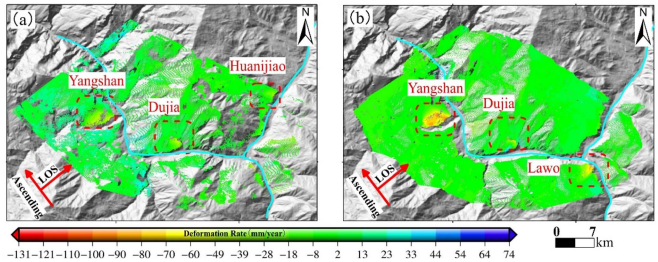

Fig. 13. Displacement velocity map derived from (a) Sentinel-1 data and (b) ALOS-2 data.

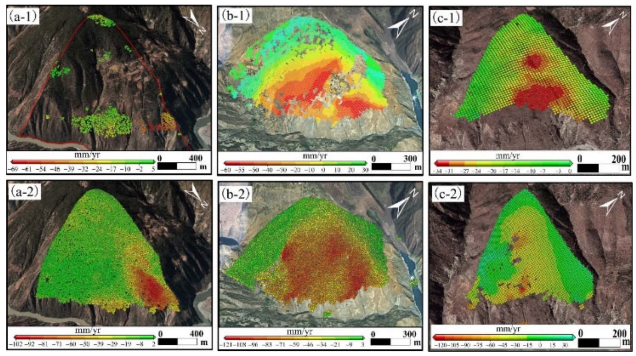

Fig. 14. Displacement velocity of the (a) Lawo slope, (b) Yangshan slope, and (c) Huanijiao slope identified by the Sentinel-1 data (upper row) and ALOS-2 data (lower row).

pairs with similar spatial baselines. The temporal baseline of Sentinel-1 is lower than ALOS-2.

The first experiment is for the area covered by dense low shrubs [see Fig. 12(a-1)]. The interferogram of Sentinel-1 data for this area has no coherence but that of the ALOS-2 data has high coherence, as shown in Fig. 12(a-2)–(a-5). The second experiment is for the area with bare slope. Both data could achieve high coherence interferograms, shown in Fig. 12(b-2)–(b-5). The third experiment is for the area covered by a medium dense broad-leaved forest. The layers of the forest are complex and continuous, and each layer is dense, resulting in poor penetration of *C* and *L* bands, so the coherence of both datasets is low, Fig. 12(c-2)–(c-5). These results lead to a conclusion: ALOS-2 data have better recognition results than Sentinel-1 in the densely vegetated areas.

2) Comparison of Displacement Results: The area (the blue rectangle in Fig. 1) covered by both the Sentinel-1 and ALOS-2 data was selected to compare the applicability of different satellite data. The ascending orbit data of the two images are processed by the same technology (SBAS-InSAR).

The results of the time series analysis are shown in Fig. 13. Sentinel-1 data identified three slopes (Yangshan, Dujia, and Huanijiao) and ALOS-2 data also identified three slopes (Yangshan, Dujia, and Lawo). The difference of the identification results is due to the different penetration of the wavelengths. In the densely vegetated area, like Lawo slope, ALOS-2 has stronger penetration to the vegetation, so it acquired dense data points. In the case of sparse vegetation, due to the shorter wavelength, Sentinel-1 data are more capable of monitoring small-scale displacement, so it identifies the Huanijiao slope.

The Lawo slope [see Fig. 14(a-1) and (a-2)] has almost complete vegetation coverage on the top but little vegetation in the middle part, where the slope is gentle with farmhouses and reclaimed farmland. The lower part is not covered by vegetation and the slope is steep (81.6°). As Fig. 14(a-2) shows, the ALOS-2 data can cover the whole slope except the foot part that belongs to the geometric distortion (shadow) area, as it is steep and is eroded by the river. In contrast, the Sentinel-1 data are greatly affected by the vegetation on the top of the slope, and get a few detection points on the bare ground in the middle of the slope body. Due to the geometric distortion, the Sentinel-1 data cannot get the displacement at the foot of the slope [see Fig. 14(a-1)]. Therefore, ALOS-2 data have better recognition for slopes with dense vegetation.

As Fig. 14(b-1) and (b-2) shows, most of the Yangshan slope is exposed. Both Sentinel-1 and ALOS-2 data can get enough detection points but Sentinel-1 data have less detection points in the vegetation-covered area than ALOS-2 data. Therefore, in the areas with medium coherence, ALOS-2 has denser effective displacement point coverage and higher detection accuracy.

The detection results of slope Huanijiao are shown in Fig. 14(c-1) and (c-2). Sentinel-1 results show obvious displacement signals while the ALOS-2 results do not show a clear signal. This is because the displacement magnitude is too small to be detected by the ALOS-2 satellite. Therefore, the Sentinel-1 data have higher detection accuracy for slopes with small displacement magnitudes. The applicability of Sentinel-1 and ALOS-2 data is summarized as shown in Table IV. It should be noted that the time span of Sentinel-1 data and ALOS-2 data is not identical, which may have the influence on the displacement

TABLE IV
SUMMARY OF THE APPLICABILITY OF *C*/*L* BANDS IN THIS STUDY

Band	C	L
Wavelength	5.6 cm	23.6 cm
SAR Satellite	Sentinel-1	ALOS-2
Vegetation Penetration	Medium	Strong
Scope of application	Large-scale and slight displacement monitoring in mountainous areas with sparse vegetation	Significant displacement monitoring in mountainous areas with dense vegetation

value. Therefore, we focus on comparing the results spatially, instead of the absolute displacement value.

VI. CONCLUSION

In this study, we use Sentinel-1 ascending and descending data to identify the potential landslides in the Yalong River alpine valley region by using SBAS-InSAR. As a result, six potential landslides were identified, which were compared with optical remote sensing images for verification.

The applicability analysis is performed considering geometric distortion and band suitability, demonstrating the use of InSAR for potential landslide identification in the alpine-canyon terrain area. The main findings and conclusions are as follows.

1) In the study area, using the combined ascending/descending data can increase the detectable area to 92.9%, which is 20% higher than that observed by either of the data. The ascending/descending SAR data are complementary in detecting the potential landslides affected by geometric distortions. Therefore, combined use of ascending and descending data is necessary while identifying and monitoring potential landslides in alpine-canyon terrain to reduce the influence of side-looking of SAR systems.
2) In terms of the coherence from different SAR sensors, the coherence of Sentinel-1 data is much lower than that of the ALOS-2 data, which means in the area with dense vegetation, ALOS-2 results have better performance to identify the spatial detailed slope displacement. On the other hand, it was found that Sentinel-1 data have better performance in identifying slopes with slight displacement because of its relatively shorter wavelength.

REFERENCES

[1] R. Liang et al., "Distribution characteristics and influencing factors analysis of geological disasters in Kala section along Yalong River," *Pearl River*, vol. 37, pp. 13–17, 2006, doi: 10.3969/j.issn.1001-9235.2016.11.00.

[2] Z. Liu, "Hazard assessment of geological disasters in the Yalong River basin from the Maidilong to Kala," M.S. thesis, Chengdu Univ. Technol., Chengdu, China, 2015.

[3] X. Chang et al., "Distribution characteristics and influencing factors of geological hazards in Yalong River basin," *J. Catastrophol.*, vol. 24, pp. 83–88, 2009, doi: 10.3969/j.issn.1000-811X.2009.03.017.

[4] K. Wang et al., "Formation process of Tanggudong landslide and Yuri accumulation body in Yalong River valley in Southwest China," *J. Eng. Geol.*, vol. 20, no. 6, pp. 955–970, 2012.

[5] Yalong River Hydropower Development Company, Ltd, Basin Overview, 2022. [Online]. Available: https://www.ylhdc.com.cn/gtylj/gsyw/lykf/lygk/A37020201index_1.html

[6] D. Ge et al., "Early identification of serious geological hazards with integrated remote sensing technologies: Thoughts and recommendations," *Geomatics Inf. Sci. Wuhan Univ.*, vol. 44, no. 7, pp. 949–956, 2019.

[7] B. Casson et al., "Contribution of multi-temporal remote sensing images to characterize landslide slip surface–application to the La Clapière landslide (France)," *Natural Hazards Earth Syst. Sci.*, vol. 5, no. 3, pp. 425–437, 2005.

[8] F. Mondini et al., "Semi-automatic recognition and mapping of rainfall induced shallow landslides using optical satellite images," *Remote Sens. Environ.*, vol. 115, no. 7, pp. 1743–1757, 2011.

[9] J. Corominas et al., "Measurement of landslide displacements using a wire extensometer," *Eng. Geol.*, vol. 55, no. 3, pp. 149–166, 2000.

[10] S. Uhlemann et al., "Assessment of ground-based monitoring techniques applied to landslide investigations," *Geomorphology*, vol. 253, pp. 438–451, 2016.

[11] M. Barla and F. Antolini, "An integrated methodology for landslides' early warning systems," *Landslides*, vol. 13, no. 2, pp. 215–228, 2016.

[12] M. Peyret et al., "Monitoring of the large slow Kahrod landslide in Alborz mountain range (Iran) by GPS and SAR interferometry," *Eng. Geol.*, vol. 100, no. 3/4, pp. 131–141, 2008.

[13] K. Dai et al., "Entering the era of earth observation-based landslide warning systems: A novel and exciting framework," *IEEE Geosci. Remote Sens. Mag.*, vol. 8, no. 1, pp. 136–153, Mar. 2020.

[14] L. Zhang et al., "Identifying potential landslides by stacking-InSAR in Southwestern China and its performance comparison with SBAS-InSAR," *Remote Sens.*, vol. 13, no. 18, 2021, Art. no. 3662.

[15] R. Tomás et al., "Spatiotemporal characteristics of the Huangtupo landslide in the three Gorges region (China) constrained by radar interferometry," *Geo-Phys. J. Int.*, vol. 197, no. 1, pp. 213–232, 2014.

[16] Q. Zhu, "Study on the landslide information extraction in Bailongjiang Basin using SBAS technique," M.S. thesis, Nanjing Normal Univ., Nanjing, China, 2015.

[17] Q. Sun et al., "Towards slow-moving landslide monitoring by integrating multi-sensor InSAR time series datasets: The Zhouqu case study, China," *Remote Sens.*, vol. 8, no. 11, 2016, Art. no. 908.

[18] K. Dai et al., "Early identification of potential landslide geohazards in alpine-canyon terrain based on SAR interferometry—A case study of the middle section of Yalong River," *J. Radars*, vol. 9, no. 3, pp. 554–568, 2020.

[19] X. Liu et al., "Integration of Sentinel-1 and ALOS/PALSAR-2 SAR datasets for mapping active landslides along the Jinsha River corridor, China," *Eng. Geol.*, vol. 284, 2021, Art. no. 106033.

[20] Y. Wang et al., "On the applicability of satellite SAR interferometry to landslide hazards detection in hilly areas: A case study of Shuicheng, Guizhou Southwest China," *Landslides*, vol. 18, pp. 2609–2619, 2021.

[21] J. Dun et al., "Detection and mapping of active landslides before impoundment in the Baihetan Reservoir Area (China) based on the time-series InSAR method," *Remote Sens.*, vol. 13, no. 16, 2021, Art. no. 3213.

[22] Y. Zhu et al., "Detection and characterization of active landslides with multisource SAR data and remote sensing in western Guizhou, China," *Natural Hazards*, vol. 111, no. 1, pp. 973–994, 2022.

[23] P. Berardino, G. Fornaro, R. Lanari, and E. Sansosti, "A new algorithm for surface deformation monitoring based on small baseline differential SAR interferograms," *IEEE Trans. Geosci. Remote Sens.*, vol. 40, no. 11, pp. 2375–2383, Nov. 2002.

[24] K. Dai et al., "Quantitative analysis of Sentinel-1 imagery geometric distortion and their suitability along Sichuan-Tibet Railway," *Geomatics Inf. Sci. Wuhan Univ.*, vol. 46, pp. 1450–1460, 2021.

[25] C. Colesanti and J. Wasowski, "Investigating landslides with space-borne synthetic aperture radar (SAR) interferometry," *Eng. Geol.*, vol. 88, no. 3/4, pp. 173–199, 2006.

[26] G. Liu et al., "New and potential technology for observation of earth from space: Synthetic aperture radar interferometry," *Adv. Earth Sci.*, vol. 6, pp. 734–740, 2000.

[27] M. Simons and P. Rosen, "Interferometric synthetic aperture radar geodesy," *Geodesy*, vol. 3, pp. 391–446, 2007.

[28] G. Liu et al., *InSAR Principles and Applications*. Beijing, China: Sci. Press, 2019.